

Passive Flow Control for the Load Reduction of Transonic Launcher Afterbodies

Scharnowski, Sven; Bosyk, Mickael; Schrijer, Ferdinand; van Oudheusden, Bas

DOI

[10.2514/1.J057357](https://doi.org/10.2514/1.J057357)

Publication date

2019

Document Version

Final published version

Published in

AIAA Journal: devoted to aerospace research and development

Citation (APA)

Scharnowski, S., Bosyk, M., Schrijer, F., & van Oudheusden, B. (2019). Passive Flow Control for the Load Reduction of Transonic Launcher Afterbodies. *AIAA Journal: devoted to aerospace research and development*, 57(5), 1818-1825. <https://doi.org/10.2514/1.J057357>

Important note

To cite this publication, please use the final published version (if applicable).
Please check the document version above.

Copyright

Other than for strictly personal use, it is not permitted to download, forward or distribute the text or part of it, without the consent of the author(s) and/or copyright holder(s), unless the work is under an open content license such as Creative Commons.

Takedown policy

Please contact us and provide details if you believe this document breaches copyrights.
We will remove access to the work immediately and investigate your claim.

Green Open Access added to TU Delft Institutional Repository

'You share, we take care!' - Taverne project

<https://www.openaccess.nl/en/you-share-we-take-care>

Otherwise as indicated in the copyright section: the publisher is the copyright holder of this work and the author uses the Dutch legislation to make this work public.



Passive Flow Control for the Load Reduction of Transonic Launcher Afterbodies

Sven Scharnowski*

Bundeswehr University Munich, 85577 Neubiberg, Germany

Mickael Bosyk†

Paris–Sorbonne University, 75005 Paris, France

and

Ferry F. J. Schrijer‡ and Bas W. van Oudheusden§

Delft University of Technology, 2629 HS Delft, The Netherlands

DOI: 10.2514/1.J057357

The base flow of an axisymmetric generic space launcher model is investigated experimentally by means of particle image velocimetry and dynamic pressure measurements at a Mach number of 0.76 and a Reynolds number of 1.5×10^6 , based on the main body diameter. The flow separation at the end of the main body forms a highly dynamic recirculation region with strong pressure fluctuations on the reattaching surface. The time-averaged reattachment on the rear sting is at 1.05 main body diameters downstream of the step. This work investigates the application of passive flow control devices for their potential of reducing the loads on the space launcher's nozzle. It is shown that rectangular or circular grooves at the end of the main body force enhanced mixing in the separated shear layer, leading to a reduction of the reattachment length of 55%. Additionally, the fluctuations of the reattachment are significantly reduced, which results in lower-pressure fluctuations and thus reduced dynamic loads.

Nomenclature

C_p	=	pressure coefficient
D	=	main body diameter, m
f	=	frequency, Hz
H_{12}	=	boundary-layer shape factor
h	=	step height, m
p	=	pressure, bar
p_0	=	stagnation pressure, bar
p_∞	=	freestream pressure, bar
PSD	=	power spectral density, Hz^{-1}
TKE	=	turbulent kinetic energy, $\text{m}^2 \cdot \text{s}^{-2}$
u, v, w	=	velocity components, $\text{m} \cdot \text{s}^{-1}$
u_∞	=	freestream velocity, $\text{m} \cdot \text{s}^{-1}$
\bar{u}	=	mean streamwise velocity, $\text{m} \cdot \text{s}^{-1}$
$\overline{u'^2}, \overline{v'^2}, \overline{w'^2}$	=	velocity fluctuations, $\text{m}^2 \cdot \text{s}^{-2}$
u_τ	=	friction velocity, $\text{m} \cdot \text{s}^{-1}$
x, y, z	=	spatial coordinates, m
x_r	=	mean reattachment length, m
δ_w	=	vorticity thickness, m
δ_1	=	displacement thickness, m
δ_2	=	momentum thickness, m
δ_{99}	=	boundary-layer thickness, m
μ	=	dynamic viscosity, $\text{Pa} \cdot \text{s}$
ρ_∞	=	freestream density, $\text{kg} \cdot \text{m}^{-3}$
τ_w	=	wall shear stress, $\text{N} \cdot \text{m}^{-2}$

I. Introduction

FLOW separation is frequently found in aerospace technology and increases the complexity of the involved flowfield. In the

case of a backward-facing step (BFS), the separation location is fixed at the trailing edge of the step, but the reattachment process is characterized by strong dynamics. In the early separated shear layer, eddies are generated due to Kelvin–Helmholtz instabilities. They become larger as they move downstream, causing the shear layer to broaden with increasing distance from the step. Additionally, the eddies become fully three-dimensional [1], and because of turbulent mixing, high-momentum fluid is transported toward the downstream surface, causing the shear layer to reattach again. For transonic Mach numbers, the vortex shedding does not happen at a fixed frequency but is usually related to a rather broad peak [2–11].

For a two-dimensional backward-facing step, the mean reattachment length is typically between $x_r = 5h$ and $7h$, with h being the step height, for the case of a fully turbulent incoming flow state at the point of separation and a Reynolds number range of $Re_h = 3000\text{--}300,000$ [12,13]. For an axisymmetric BFS, the mean reattachment length is reduced to values between $1.0D$ and $1.1D$ (corresponding to $3.3h$ and $3.6h$) for experiments at a Reynolds number range of $Re_D = (1.1\text{--}1.5) \times 10^6$ [4,14,15]. The reattachment location fluctuates in space and time due to the dynamics of turbulent structures. For a two-dimensional BFS flow, the instantaneous impingement location of the shear layer moves up- and downstream by as much as $\pm 3h$ [1,16]. Weiss and Deck [17] as well as Schrijer et al. [18] showed that the instantaneous reattachment location also strongly varies for an axisymmetric model. As a result, the reattaching surface is subject to strong pressure fluctuations that might interfere with structural modes leading to so-called buffeting.

One famous example of a BFS in aerospace technology is the base geometry of the European space launcher Ariane 5; see Fig. 1. At the end of the cylindrical main body, a BFS configuration can be observed in the transition to the main engine's nozzle. The length and diameter of the nozzle are such that the separated shear layer reattaches close to the end of the nozzle, causing high dynamic loads [6–8,19–23]. A reduction of the pressure fluctuations is desirable to increase the safety margins. This would possibly enable to use a longer and larger nozzle to improve the overall performance.

Different passive flow control devices were tested in the past to reduce the structural loads [8,24,25]. One approach is to delay separation and consequently move the reattachment location toward the exhaust plume. This can be achieved by adding a skirt at the end of the main body [8,24]. Another approach is to shorten the reattachment length, which potentially reduces the fluctuations at the end of the nozzle. Hannemann et al. [8] used a so-called scoop on an

Received 29 March 2018; revision received 13 November 2018; accepted for publication 23 November 2018; published online 31 December 2018. Copyright © 2018 by the American Institute of Aeronautics and Astronautics, Inc. All rights reserved. All requests for copying and permission to reprint should be submitted to CCC at www.copyright.com; employ the eISSN 1533-385X to initiate your request. See also AIAA Rights and Permissions www.aiaa.org/randp.

*Research Associate, Institute of Fluid Mechanics and Aerodynamics, Werner-Heisenberg-Weg 39.

†Master Student, Department of Fluid Mechanics, 4 Place Jussieu.

‡Assistant Professor, Department of Aerospace Engineering, Kluuyverweg 1.

§Associate Professor, Department of Aerospace Engineering, Kluuyverweg 1.

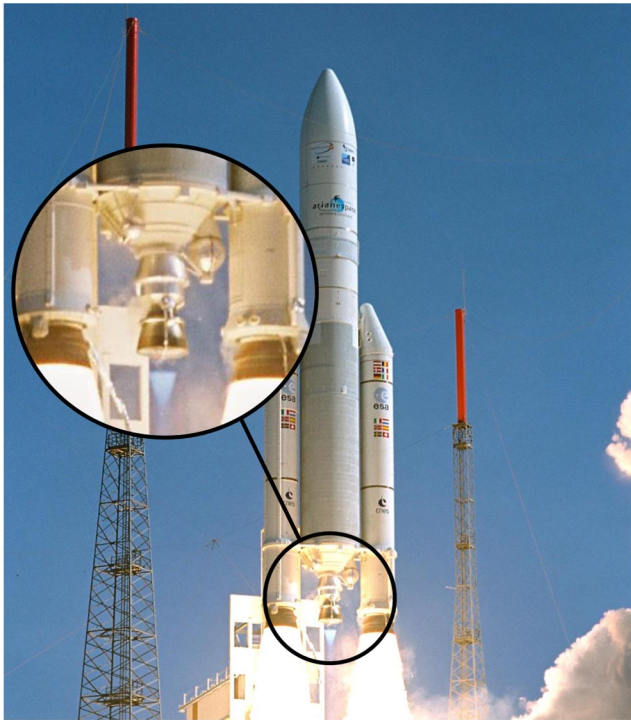


Fig. 1 European space launcher Ariane 5 during lift-off (image provided by the European Space Agency).

Ariane 5 model to deflect the flow at the rear end inward. This significantly reduces pressure fluctuations on the nozzle but also increases aerodynamic drag. Schrijer et al. [25] tested chevron-type flow control devices (skirts with toothed trailing edge) to enhance mixing in the shear layer. Although the chevron devices are of three-dimensional nature, the majority of the chevron configurations were found to result in a statistically axisymmetric flowfield. The addition of the devices to a clean base increases the velocity fluctuations slightly, and larger backflow velocities are measured. Chevron-type flow control devices have also been studied for jet flows in [26] and for afterbody flows in [27]. More recently, it was shown that convoluted trailing edges, by means of circular or squared lobes, are able to reduce the reattachment length as well as the loads due to wall pressure fluctuations significantly in the case of a planar backward-facing step [15,28,29]. Although these lobes efficiently enhance mixing, their protruding peaks increase the aerodynamic drag. Based on these findings in [29], passive flow control devices that only contain the valleys are investigated on an axisymmetric model in this work.

II. Experimental Setup

The experiments were performed in the transonic-supersonic wind tunnel (TST-27) of the High-Speed Aerodynamics Laboratories at Delft University of Technology. The TST-27 facility is a blowdown-type wind tunnel with a 28-cm-wide and 27-cm-high test section. Details about this facility can be found in [25]. For the present experiments, the wind tunnel is operated at a nominal Mach number of 0.7, which approaches 0.76 on the main body of the model. With a total pressure of $p_0 = 2.00$ bar, a Reynolds number based on the main body diameter $D = 50$ mm of $Re_D = 1.5 \times 10^6$ was achieved.

The generic space launcher model consists of a cylindrical main body with a gently curved nose and a rear sting, which is used to mount the model in the test section. The diameters of the main body and the sting are 50 and 20 mm, respectively, leading to a step height of 15 mm at the end of the main body. The model size is a compromise between blockage and sufficient size for instrumentation. A smaller model would be advantageous to reduce blockage effects but does not allow the placement of sensors, which are important for the

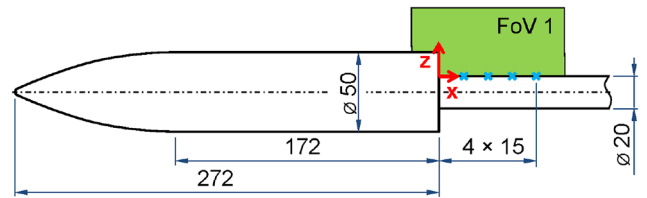


Fig. 2 Sketch of the wind-tunnel model with field of view 1 for the PIV measurements. Numerical values are given in millimeters.

assessment of the loads. Figure 2 shows a sketch of the model together with the field of view (FOV 1) for flowfield measurements on the plane of symmetry. In the figure, the crosses on the top side of the sting mark the locations of dynamic pressure sensors. At the rear end of the main body, exchangeable rings were used to mount the different flow control devices. Besides the clean case with a sharp trailing edge, a ring with rectangular grooves and one with circular grooves were investigated. A total number of 13 grooves with a depth of $0.06D$, a width of $0.12D$, and an inclination of 18 deg were distributed over the circumference. By selecting an odd number of grooves, the triggering of certain circumferential modes is suppressed. The flow control rings can be rotated to have the dynamic pressure sensors and the particle image velocimetry (PIV) measurement plane downstream of a groove or downstream of a location between the grooves. The former measurement plane is in the following referred to as the valley and the latter as the peak. Figure 3 illustrates the three exchangeable rings.

Stereoscopic PIV was used to capture the wake flow in two orthogonal planes. The plane of symmetry (FOV 1) captures the evolution of the separated shear layer as well as the dynamics of the recirculation bubble. A second field of view (FOV 2) investigated a spanwise plane at $x/D = 0.6$ to characterize the circumferential variations of the shear layer. For the PIV measurements in FOV 1 and FOV 2, two LaVision Imager LX 2MP cameras with a sensor size of 1628×1236 pixels were used together with 60 mm focal length lenses in a stereoscopic configuration to capture all three velocity components in the separated region. For FOV 1, an additional camera with a 105 mm lens resolved the incoming boundary layer on the model main body. The flow was seeded with di-ethyl-hexyl-sebacat droplets with a mean diameter of $1 \mu\text{m}$ [30]. The size of the tracers is a compromise between visibility and the ability to follow the flow. The response time of these droplets is about $2 \mu\text{s}$ [31], which is considered to be sufficient for investigations at the selected Mach and Reynolds number. The tracers were illuminated with a ~ 1 mm-thick light sheet generated by a 400 mJ double-pulse laser (Quanta-Ray by Spectra Physics).

With this PIV setup, a mean particle image diameter of about 2.0 pixels was achieved. After image preprocessing, including background subtraction and particle image intensity normalization, a background noise level with a standard deviation of ~ 5 counts was estimated from the autocorrelation function with the method presented in [32]. This noise level leads to a loss of correlation due to image noise of $F_\sigma \approx 0.85$ and to a signal-to-noise ratio of $\text{SNR} \approx 2.0$ based on the findings in [32], which is considered to be well suited for PIV evaluation. Up to 500 PIV double stereo images were recorded at statistically independent time steps with a recording frequency of 10 Hz. The time separation between the double images was set to $2.0 \mu\text{s}$ for FOV 1 to ensure a maximum particle image shift of less

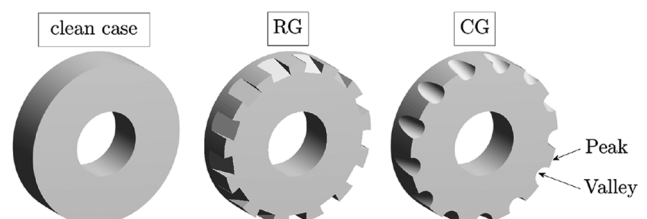


Fig. 3 Exchangeable trailing edge rings of the model: clean case (left), rectangular grooves (middle), and circular grooves (right).

than 12 pixels. This shift allows precise flowfield measurements without strong bias errors due to curved streamlines [33]. For the spanwise plane, where the main flow direction is the out-of-plane direction, the time separation was reduced to $0.75 \mu\text{s}$ to ensure a sufficiently small amount of loss of pairs for reliable velocity estimation, according to [34,35]. For the data evaluation, iterative window correlation including image deformation and Gaussian window weighting was applied. The final interrogation-window size was set to 24×24 or 64×64 pixel with an overlap of 50% for FOV 1 and FOV 2, respectively. The resulting vector grid spacing is about $500 \mu\text{m}$ (or 1% of the main body diameter) for FOV 1 and two times larger for FOV 2. In a postprocessing step, vectors that differ by more than two times the standard deviation of their neighbors from the median of the neighbors (for each component) were considered to be outliers [36] and were therefore rejected before computing mean fields and turbulence levels. The incoming boundary layer was evaluated by means of single-pixel ensemble correlation, which results in an improved spatial resolution, as discussed in [37–40]. The resulting vector grid spacing is about $16 \mu\text{m} \approx 0.0003D$ for this evaluation approach.

To evaluate the dynamic loads of the reattaching shear layer, PIV was complemented with pressure measurements on the sting at four locations (one, two, three, and four step heights, $x/D = 0.3, 0.6, 0.9$, and 1.2) downstream of the step, by means of dynamic pressure transducers (Endevco 8507C, range: 1 bar). The pressure sensors were flush-mounted, and the signals were read out at 50 kHz.

III. Results and Discussion

A. Incoming Boundary Layer

For the presented BFS flow, the incoming boundary layer is characterized on the main body at a location one step height upstream of the step ($x/D = -0.3$). Figure 4 illustrates the mean streamwise velocity profile at that location $\bar{u}(z)$ normalized by the freestream velocity $u_\infty = 237 \text{ m} \cdot \text{s}^{-1}$. The boundary-layer thickness is $\delta_{99}/D = 0.06 \pm 0.0015$. The first reliable measurement point of the profile in Fig. 4 is located $65 \mu\text{m}$ above the wall, which is assumed to be on the edge of the buffer layer. Extrapolating the velocity toward the wall with a linear profile allows to estimate the (incompressible) displacement and momentum thickness. The displacement thickness at $x/D = -0.3$ is

$$\frac{\delta_1}{D} = \frac{1}{D} \int_{D/2}^{\infty} \left[1 - \frac{\bar{u}(z)}{u_\infty} \right] dz \approx 0.0087 \quad (1)$$

and the momentum thickness is

$$\frac{\delta_2}{D} = \frac{1}{D} \int_{D/2}^{\infty} \frac{\bar{u}(z)}{u_\infty} \left[1 - \frac{\bar{u}(z)}{u_\infty} \right] dz \approx 0.0066 \quad (2)$$

Thus, the Reynolds number based on the momentum thickness and the shape factor are $Re_{\delta_2} \approx 9900$ and $H_{12} = \delta_1/\delta_2 \approx 1.32$, respectively. Consequently, it can be concluded that the boundary

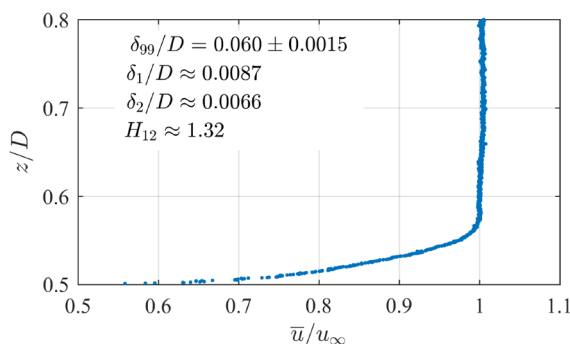


Fig. 4 Incoming mean streamwise velocity profile measured at $x/h = -0.3$. The velocity was normalized with the freestream velocity $u_\infty = 237 \text{ m} \cdot \text{s}^{-1}$.

layer at the end of the main body is fully turbulent for the analyzed Mach and Reynolds number combination, according to [41].

According to Bradshaw and Wong [12], this incoming boundary layer is subject to an overwhelming perturbation because the ratio between step height and boundary-layer thickness is $h/\delta \approx 5$. Thus, the strength and thickness in the initial shear layer at the point of separation are mainly determined by the high velocity gradient in the near-wall region of the incoming boundary layer.

From the last data points, the near wall gradient was determined to be $\partial u/\partial z|_{z \rightarrow D/2} > 2.1 \cdot 10^6 \text{ s}^{-1}$. Hence, the wall shear stress was estimated to

$$\tau_w = \lim_{z \rightarrow D/2} \mu \cdot \partial \bar{u}/\partial z > 32 \text{ N m}^{-2} \quad (3)$$

the friction velocity is

$$u_\tau = \sqrt{\tau_w/\rho_\infty} > 4.0 \text{ m s}^{-1} \quad (4)$$

and the skin friction coefficient is

$$C_f = \frac{\tau_w}{1/2 \rho_\infty \cdot u_\infty^2} > 5.8 \cdot 10^{-4} \quad (5)$$

where the viscosity and the density are $\mu = 1.55 \times 10^{-5} \text{ Pa} \cdot \text{s}$ and $\rho_\infty = 1.96 \text{ kg} \cdot \text{m}^{-3}$, respectively.

B. Plane of Symmetry

For the clean case, the time-averaged velocity distribution forms a large separation bubble downstream of the step, as illustrated in the top row of Fig. 5. The mean reattachment length is 3.5 step heights or 1.05 main body diameters, which is in agreement with other experiments [4,14,42] and numerical simulations [7,11,43] at similar flow conditions. The flow topology totally changes for the controlled cases with rectangular and circular grooves, as shown in the middle and bottom rows of Fig. 5, respectively. The corrugated shape of the trailing edge forces the generation of streamwise aligned vortices, which enhance mixing in the separated shear layer. As a result, the mean reattachment length reduces to $0.48D$ for both geometries for a location downstream of a peak of the flow control rings. Behind the grooves, reattachment occurs even earlier ($0.41D$ for circular grooves and $0.47D$ for rectangular grooves), which is in agreement with the findings in [29]. The strongly spiralized streamlines in the separated regions of the controlled cases are clear evidence of the three-dimensionality of the time-averaged flowfield.

Because of the mixing within the separated shear layer, the gradient $\partial_z \bar{u}$ decreases rapidly. From the mean velocity distribution in Fig. 5, the development of the maximum gradient was extracted and is illustrated in Fig. 6 in the top row. In the first part of the separated region, the shear-layer gradient is similar for all cases. But in the region $0.25 \leq x/D \leq 0.6$, the shear layer gradients for the controlled cases are up to 30% higher than for the clean case, whereas farther downstream, the controlled cases show smaller values. It is important to note that the maximum gradient within the separated shear layer is used for this analysis rather than that near the wall of the sting in the newly developing boundary layer.

From the shear-layer gradient and the difference between maximum and minimum mean velocity at fixed streamwise location, the vorticity thickness is computed as follows:

$$\delta_\omega(x) = \frac{u_{\max}(x) - u_{\min}(x)}{\max[\partial_z \bar{u}](x)} \quad (6)$$

The development of the vorticity thickness is given in the bottom row of Fig. 6 and follows an approximately reciprocal trend to that of the maximum velocity gradient. For the clean case and for both controlled cases, the vorticity thickness grows approximately linearly in the first half of the separated region with a similar growth rate. For the controlled cases, the growth rate decreases in the region $0.25 \leq x/D \leq 0.45$ and increases again farther downstream. For the clean

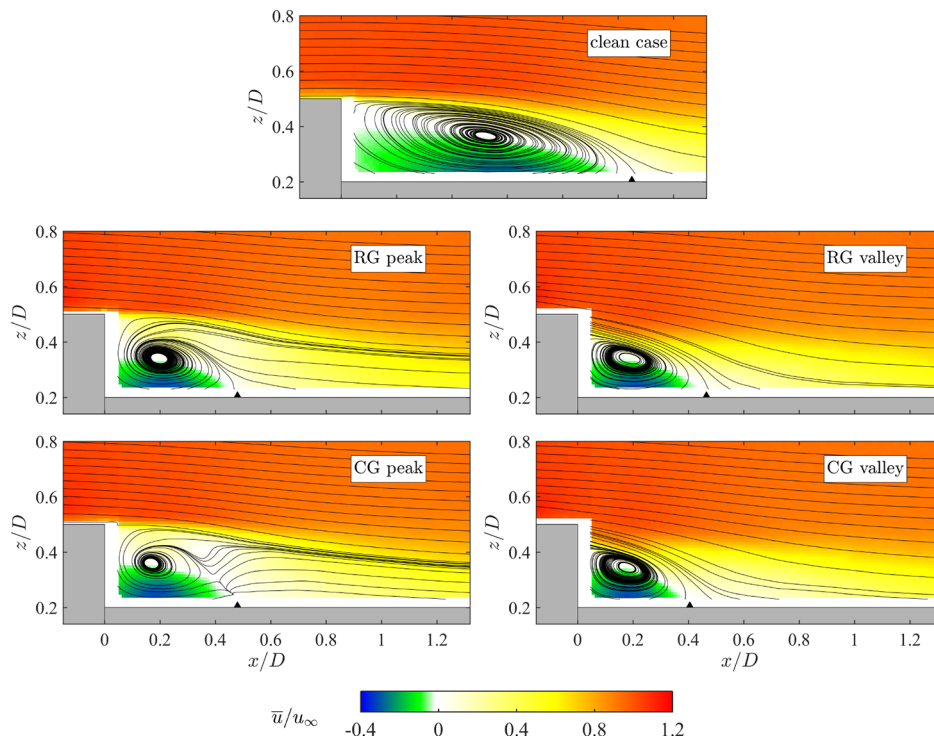


Fig. 5 Mean streamwise velocity distribution with streamlines for the clean case (top), rectangular grooves (middle), and circular grooves (bottom). The mean reattachment location is indicated by the black triangle.

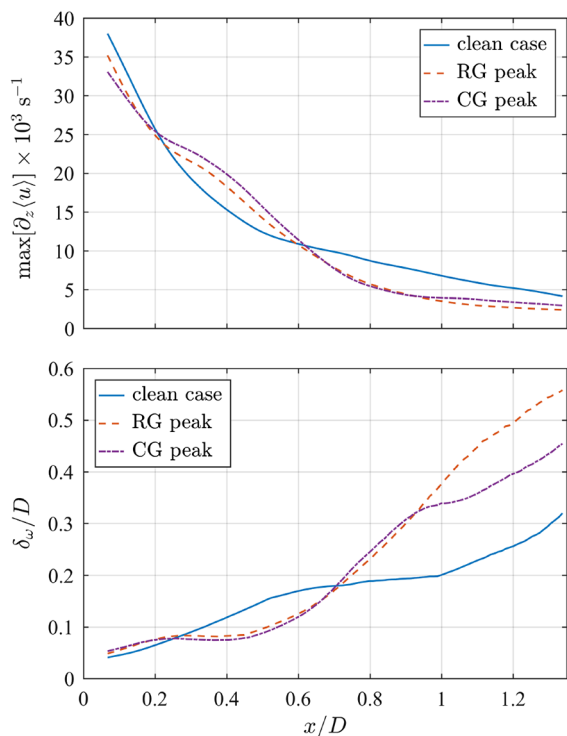


Fig. 6 Development of the maximum shear-layer gradient $\max[\partial_z \bar{u}]$ (top) and the vorticity thickness δ_ω (bottom) along the streamwise direction.

case, the development is similar but delayed. At $x/D \approx 0.7$, the curves cross each other, and the vorticity thickness of the controlled cases becomes larger than that for the clean case. Downstream of $x/D = 0.9$, the rectangular grooves (RGs) result in even larger vorticity thickness than the circular grooves (CGs). The faster growing vorticity thickness in the bottom row of Fig. 6 goes hand in hand with the faster decreasing shear-layer gradient shown from the top row of the figure and confirms the enhanced mixing for the controlled cases.

Regarding the instantaneous dynamics, the separated shear layer is subject to strong velocity fluctuations induced by shear-layer vortices and shear-layer fluctuations, as discussed in Sec. I. The velocity fluctuations of the clean case model, shown in the top row of Fig. 7, are characterized by high values in a broad region around the reattachment location ($0.6 \leq x/D \leq 1.2$), as expected. The spatial distributions for all three normal stress components are similar in shape. However, it is interesting to note that the fluctuations in the circumferential direction v'^2 are much stronger than those in the radial direction w'^2 . This indicates an early breakdown of the shear-layer vortices and the generation of fully three-dimensional structures.

Also for the controlled cases, the spatial distributions of the stress components in the second-to-bottom row of Fig. 7 show the largest fluctuations in a region around the mean reattachment. However, because of the fact that reattachment occurs much earlier for the controlled cases, the stress levels downstream of $x/h \approx 0.6$ are significantly reduced compared to the clean case. Within the separated region as well as in the early shear layer, the fluctuation of the streamwise velocity component u'^2 is even stronger than that for the clean case model. On the one hand, the fluctuations of the circumferential velocity component v'^2 behind the peak do not show as high values as for the clean case. And on the other hand, the fluctuations of the radial component w'^2 are significantly higher than for the uncontrolled case. Thus, the rectangular and circular grooves significantly change the wake flow topology. The enhanced mixing causes the region of high fluctuation to be compressed in the longitudinal direction.

C. Spanwise Plane

To analyze the effect of the flow control devices in the azimuthal direction, a spanwise plane at $x/D = 0.6$ was investigated. At this streamwise location, the clean case is characterized by strong reversed flow, whereas for the controlled cases, the shear layer is already reattached. Note that, for the controlled cases, the vertical axis ($y = 0$) would intersect the control element at a peak of the geometry (compare Fig. 3). The mean velocity distribution in the left column of Fig. 8 shows reversed flow only for the clean case model, whereas in the two controlled cases, the flow is already reattached. In

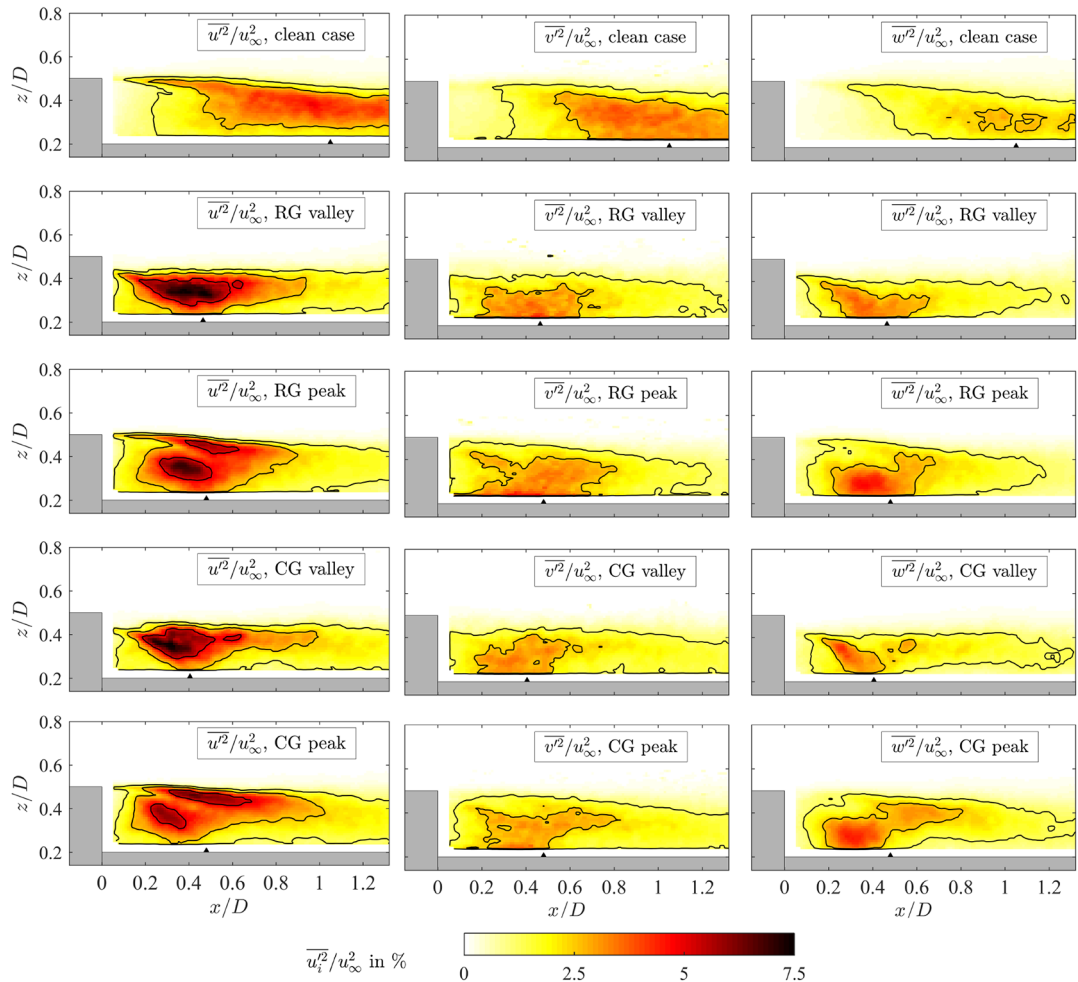


Fig. 7 Velocity fluctuations on the plane of symmetry for the clean case (top row), rectangular grooves (second and third row), and circular grooves (fourth and bottom row).

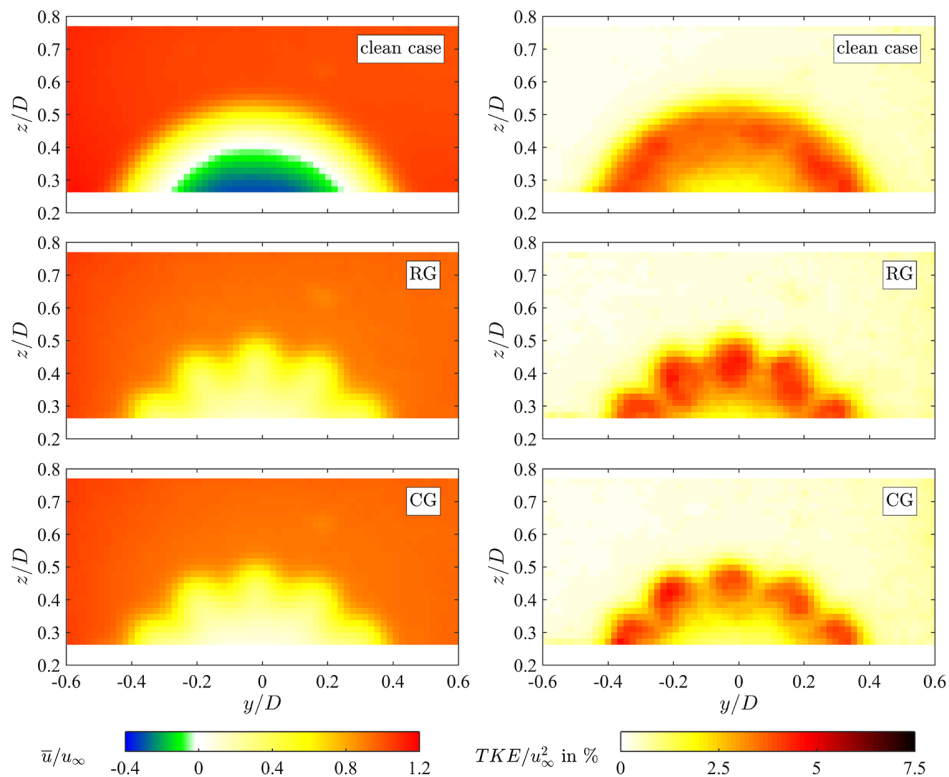


Fig. 8 Mean streamwise velocity distribution (left column) and turbulent kinetic energy (TKE, right column) for the different configurations in a spanwise plane at $x/D = 0.6$.

contrast to the clean case, which results in an axisymmetric mean flowfield, the grooves in the trailing edge lead to a three-dimensional, circumferentially periodic shape of the separated shear layer. It is interesting to note that the strongest variations of the velocity in the circumferential direction appear in the outer shear layer, whereas close to the rear sting, the distribution becomes more uniform. The right column in Fig. 8 shows the distribution of the turbulent kinetic energy (TKE):

$$TKE = 1/2(\overline{u'^2} + \overline{v'^2} + \overline{w'^2}) \quad (7)$$

Also, the TKE distribution is characterized by strong changes within the shear layer for the controlled cases. The induced streamwise aligned vortices are obviously very stable. Behind the peaks, the velocity fluctuations are significantly stronger than downstream of the grooves at $x/h = 2$. However, for the controlled cases, the maximum values of TKE are already in the same order as for the clean case. Farther downstream, TKE decreases for the controlled cases but still increases for the clean case, as can be seen from the fluctuation in Fig. 7.

D. Pressure Measurements

Whether or not the reduced reattachment length is beneficial for the loads on the rear sting, or the nozzle in the case of a space launcher, is evaluated by means of dynamic pressure measurements. The mean pressure coefficient C_p is defined as

$$C_p = \frac{p - p_\infty}{1/2\rho_\infty \cdot u_\infty^2} \quad (8)$$

where the freestream density and velocity are $\rho_\infty = 1.96 \text{ kg} \cdot \text{m}^{-3}$ and $u_\infty = 237 \text{ m} \cdot \text{s}^{-1}$, respectively. The static pressure p was averaged over 10 s, and the reference pressure p_∞ was measured on the side of the main body, three step heights upstream of the step. Figure 9 shows the mean pressure coefficient $C_{p,\text{mean}}$ and its standard deviation $C_{p,\text{rms}}$ for the four points on the rear sting. The $C_{p,\text{mean}}$ values for the clean case nicely match results from the literature [6,43], which show the maximum just downstream of the mean reattachment location. For the two controlled cases, the $C_{p,\text{mean}}$

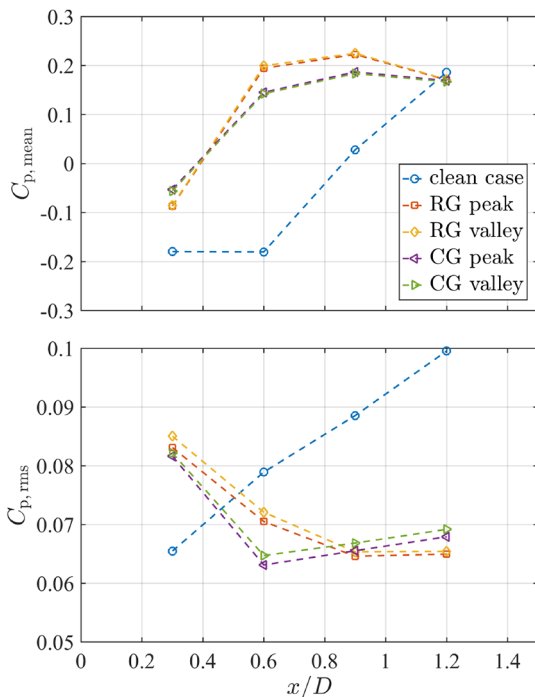


Fig. 9 Mean pressure coefficient (top) and pressure fluctuations (bottom) on the model's sting. For the controlled cases, results are shown behind the peaks and the valleys.

values are increased, and the maximum is shifted upstream, as expected due to the earlier reattachment. It is interesting to note that, for both controlled cases, almost no difference between the location behind the peaks and behind the grooves was found for all four measurement points. Thus, the strong variations in the shear layer do not lead to appreciable differences in the pressure coefficients at the surface. It is not directly evident whether the overall base drag would also be reduced by the flow control devices because the pressure on the base surface was not measured. However, measurements very close to the base of a two-dimensional BFS using similar flow control devices indicate a slight base drag reduction for the controlled cases [29].

From the bottom row in Fig. 9, it can be seen that the pressure fluctuations increase with larger distance from the step for the clean case. This is also in accordance with the sources referred to

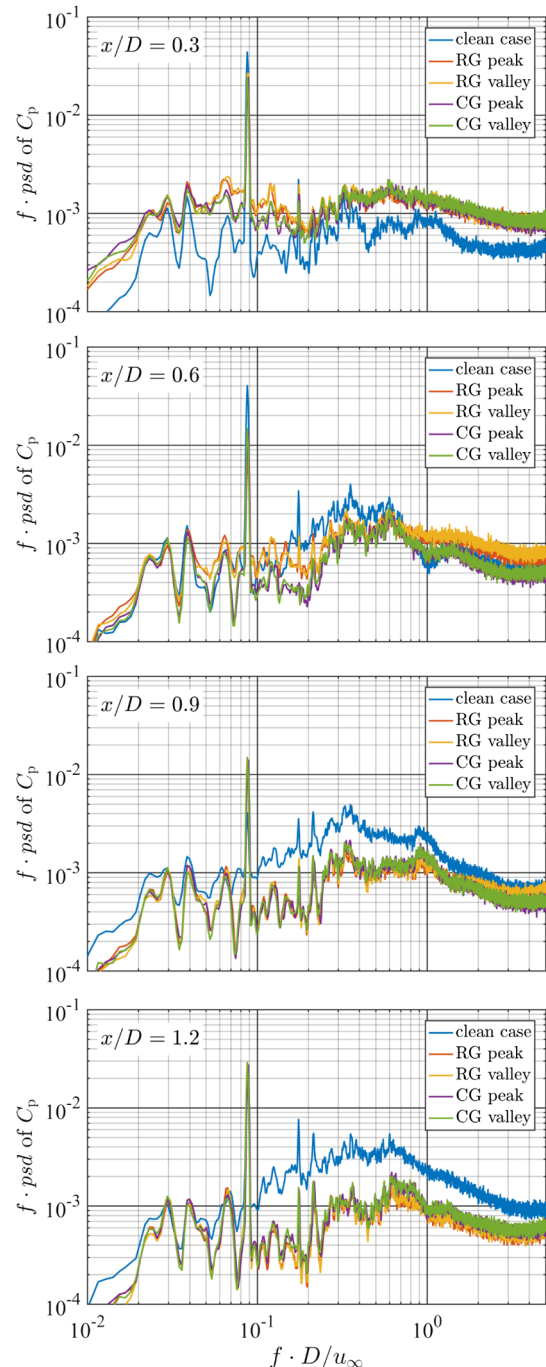


Fig. 10 Premultiplied power spectral density (PSD) of the pressure coefficient at $x/D = 0.3 \dots 1.2$ (top to bottom) for the clean case and the controlled cases (behind the peaks and the valleys).

previously, where the maximum fluctuation levels are found around the reattachment location. However, for the controlled cases, the highest fluctuations occur at $x/D = 0.3$, which is even upstream of reattachment. Furthermore, for $x/D \geq 0.6$, the pressure fluctuations of both controlled cases become smaller than those of the clean case and are reduced by as much as 35% for $x/D = 1.2$.

The reduction of the dynamic pressure fluctuations at the location of the sensors happens over a large range of frequencies, as can be seen from the premultiplied power spectral density (PSD) in Fig. 10 for the four locations $x/D = 0.3 \dots 1.2$. The spectra were computed from 500,000 data points with an acquisition rate of 50 kHz with the method of Welch [44] using a window length of 5000 data points and a Hamming window function. At $x/D = 0.3$, the pressure fluctuations for the controlled cases are significantly stronger for all frequencies. All spectra show a strong peak at $f \cdot D/u_\infty = 0.088$, which is known to be a characteristic frequency of the TST-27 wind tunnel. Besides that, a broad excitation in the range of $f \cdot D/u_\infty = 0.3$ to 1 can be observed. For $x/D = 0.6$, the pressure fluctuations of the clean case are already higher than of the controlled cases for frequencies below $f \cdot D/u_\infty = 0.8$. And for $x/D = 0.9$ and $x/D = 1.2$, the clean case shows higher values over the full range. Comparing the two groove geometries, it can be seen that the spectra are rather similar over the whole range of frequencies. The rectangular grooves result in 10% higher fluctuations at $x/D = 0.6$ and 5% lower ones at $x/D = 1.2$, consistent with the stress distributions in Fig. 7. Regarding the two locations, peak and valley, no significant difference can be observed in the spectra. It is important to note that no additional peaks are introduced by the flow control devices, which could lead to additional excitation of structural modes. Based on the overall damping of the pressure fluctuations, it is concluded that the tested geometries are potentially well suited to reduce the overall loads in realistic launcher configurations, such as on the main engine's nozzle of an Ariane 5-like space launcher during the transonic flight stage.

IV. Conclusions

It was shown that rectangular or circular grooves at the trailing edge of a space launcher model are well suited to enhance mixing in the separated shear layer. Although higher fluctuations are introduced in the near-base region, farther downstream the pressure fluctuations and velocity fluctuations are significantly reduced. The increased fluctuations close to the step are not very crucial because the momentum arm is relatively short. On the other hand, the reduced fluctuations at the longer momentum arm decrease the overall loads on the reattaching surface. Because of the limited number of pressure sensors in the model, it remains somewhat uncertain whether the overall dynamic loads could be reduced by the applied modifications [45]. However, the presented results indicate that the tested flow control devices could potentially be used to reduce mechanical loads on a space launcher's main engines nozzle during transonic flight.

The size, spacing, and shape of the grooves turned out to be rather efficient in controlling the reattaching shear layer such that it reduces the loads on the sting. It was shown that no azimuthal varying forces or specific frequencies are introduced. However, the tested flow control devices are not optimized for a realistic space launcher. To find a perfect solution, the real launcher geometry with solid-state boosters should be considered. Future work should also focus on the effect at different Mach numbers, to decide whether such flow control devices should be kept during atmospheric ascent or dropped after the transonic phase. Nevertheless, the findings clearly show the potential of passive flow control devices to improve the reliability and the performance of future space launchers.

Acknowledgments

S. Scharnowski would like to thank C. J. Kähler and F. Scarano for supporting his research stay in Delft, during which the measurements in the TST-27 facility were performed.

References

- [1] Simpson, R., "Turbulent Boundary-Layer Separation," *Annual Review of Fluid Mechanics*, Vol. 21, 1989, pp. 205–232. doi:10.1146/annurev.fl.21.010189.001225
- [2] Driver, D., Seegmiller, H., and Marvin, J., "Time-Dependent Behavior of a Reattaching Shear Layer," *AIAA Journal*, Vol. 25, No. 7, 1987, pp. 914–919. doi:10.2514/3.9722
- [3] Bitter, M., Hara, T., Hain, R., Yorita, D., Asai, K., and Kähler, C., "Characterization of Pressure Dynamics in an Axisymmetric Separating/Reattaching Flow Using Fast-Responding Pressure-Sensitive Paint," *Experiments in Fluids*, Vol. 53, No. 6, 2012, pp. 1737–1749. doi:10.1007/s00348-012-1380-7
- [4] Bitter, M., Scharnowski, S., Hain, R., and Kähler, C., "High-Repetition-Rate PIV Investigations on a Generic Rocket Model in Sub- and Supersonic Flows," *Experiments in Fluids*, Vol. 50, No. 4, 2011, pp. 1019–1030. doi:10.1007/s00348-010-0988-8
- [5] Bolgar, I., Scharnowski, S., and Kähler, C. J., "The Effect of the Mach Number on a Turbulent Backward-Facing Step Flow," *Flow, Turbulence and Combustion*, April 2018. doi:10.1007/s10494-018-9921-7
- [6] Depres, D., Reijasse, P., and Dussauge, J., "Analysis of Unsteadiness in Afterbody Transonic Flows," *AIAA Journal*, Vol. 42, No. 12, 2004, pp. 2541–2550. doi:10.2514/1.7000
- [7] Deck, S., and Thorigny, P., "Unsteadiness of an Axisymmetric Separating-Reattaching Flow: Numerical Investigation," *Physics of Fluids*, Vol. 19, No. 6, 2007, Paper 065103. doi:10.1063/1.2734996
- [8] Hannemann, K., Lüdeke, H., Pallegoix, J.-F., Ollivier, A., Lambaré, H., Maseland, J., Geurts, E., Frey, M., Deck, S., Schrijer, F., et al., "Launcher Vehicle Base Buffeting—Recent Experimental and Numerical Investigations," *Proceedings of the 7th European Symposium on Aerothermodynamics for Space Vehicles*, Bruges, Belgium, May 2011.
- [9] Statnikov, V., Bolgar, I., Scharnowski, S., Meinke, M., Kähler, C., and Schröder, W., "Analysis of Characteristic Wake Flow Modes on a Generic Transonic Backward-Facing Step Configuration," *European Journal of Mechanics—B/Fluids*, Vol. 59, No. 5, 2016, pp. 124–134. doi:10.1016/j.euromechflu.2016.05.008
- [10] Weiss, P.-E., and Deck, S., "Numerical Investigation of the Robustness of an Axisymmetric Separating/Reattaching Flow to an External Perturbation Using ZDES," *Flow, Turbulence and Combustion*, Vol. 91, No. 3, 2013, pp. 697–715. doi:10.1007/s10494-013-9484-6
- [11] Weiss, P.-E., Deck, S., Robinet, J.-C., and Sagaut, P., "On the Dynamics of Axisymmetric Turbulent Separating/Reattaching Flows," *Physics of Fluids*, Vol. 21, No. 7, 2009, Paper 075103. doi:10.1063/1.3177352
- [12] Bradshaw, P., and Wong, F., "The Reattachment and Relaxation of a Turbulent Shear Layer," *Journal of Fluid Mechanics*, Vol. 52, No. 1, 1972, pp. 113–135. doi:10.1017/S002211207200299X
- [13] Eaton, J., and Johnston, J., "A Review of Research on Subsonic Turbulent Flow Reattachment," *AIAA Journal*, Vol. 19, No. 9, 1981, pp. 1093–1100. doi:10.2514/3.60048
- [14] van Gent, P., Payanda, Q., Brust, S., van Oudheusden, B., and Schrijer, F., "Experimental Study of the Effects of Exhaust Plume and Nozzle Length on Transonic and Supersonic Axisymmetric Base Flows," *7th European Conference for Aeronautics and Space Science*, Milan, July 2017.
- [15] Scharnowski, S., Bolgar, I., and Kähler, C., "Control of the Recirculation Region of a Transonic Backward-Facing Step Flow Using Circular Lobes," *9th International Symposium on Turbulence and Shear Flow Phenomena*, Melbourne, Australia, June–July 2015.
- [16] Scharnowski, S., Bolgar, I., and Kähler, C. J., "Characterization of Turbulent Structures in a Transonic Backward-Facing Step Flow," *Flow, Turbulence and Combustion*, Vol. 98, No. 4, 2017, pp. 947–967. doi:10.1007/s10494-016-9792-8
- [17] Weiss, P.-É., and Deck, S., "Control of the Antisymmetric Mode ($m = 1$) for High Reynolds Axisymmetric Turbulent Separating/Reattaching Flows," *Physics of Fluids*, Vol. 23, No. 9, 2011, Paper 095102. doi:10.1063/1.3614481
- [18] Schrijer, F. F. J., Sciacchitano, A., and Scarano, F., "Spatio-Temporal and Modal Analysis of Unsteady Fluctuations in a High-Subsonic Base

- Flow," *Physics of Fluids*, Vol. 26, No. 8, 2014, Paper 086101. doi:10.1063/1.4891257
- [19] Pain, R., Weiss, P.-E., and Deck, S., "Zonal Detached Eddy Simulation of the Flow Around a Simplified Launcher Afterbody," *AIAA Journal*, Vol. 52, No. 9, 2014, pp. 1967–1979. doi:10.2514/1.J052743
- [20] Weiss, P.-É., and Deck, S., "On the Coupling of a Zonal Body-Fitted/Immersed Boundary Method with ZDES: Application to the Interactions on a Realistic Space Launcher Afterbody Flow," *Computers & Fluids*, Vol. 176, Nov. 2018, pp. 338–352. doi:10.1016/j.compfluid.2017.06.015
- [21] David, C., and Radulovic, S., "Prediction of Buffet Loads on the Ariane 5 Afterbody," *6th International Symposium on Launcher Technologies*, Munich, 2005.
- [22] Schrijer, F., Sciacchitano, A., Scarano, F., Hanneman, K., Pallegoix, J., Maseland, J., and Schwane, R., "Experimental Investigation of Base Flow Buffeting on the Ariane 5 Launcher Using High Speed PIV," *Proceedings of the 7th European Symposium on Aerothermodynamics for Space Vehicles*, Vol. 692, Bruges, Belgium, May 2011, p. 102.
- [23] Lüdeke, H., Mulot, J. D., and Hannemann, K., "Launch Vehicle Base Flow Analysis Using Improved Delayed Detached-Eddy Simulation," *AIAA Journal*, Vol. 53, No. 9, 2015, pp. 2452–2471. doi:10.2514/1.J053297
- [24] Depres, D., Radulovic, S., and Lambare, H., "Reduction of Unsteady Effects in Afterbody Transonic Flows," *6th International Symposium on Launcher Technologies*, Munich, 2005.
- [25] Schrijer, F., Sciacchitano, A., and Scarano, F., "Experimental Investigation of Flow Control Devices for the Reduction of Transonic Buffeting on Rocket Afterbodies," *Proceedings of the 15th International Symposium on Applications of Laser Techniques to Fluid Mechanics*, edited by C. Tropea, and R. Adrian, 2010.
- [26] Xia, H., Tucker, P. G., and Eastwood, S., "Large-Eddy Simulations of Chevron Jet Flows with Noise Predictions," *International Journal of Heat and Fluid Flow*, Vol. 30, No. 6, 2009, pp. 1067–1079. doi:10.1016/j.ijheatfluidflow.2009.05.002
- [27] Mochel, L., Weiss, P.-É., and Deck, S., "Zonal Immersed Boundary Conditions: Application to a High-Reynolds-Number Afterbody Flow," *AIAA Journal*, Vol. 52, No. 12, 2014, pp. 2782–2794. doi:10.2514/1.J052970
- [28] Bolgar, I., Scharnowski, S., and Kähler, C. J., "Control of the Reattachment Length of a Transonic 2D Backward-Facing Step Flow," *Proceedings of the 5th International Conference on Jets, Wakes and Separated Flows*, Springer, Cham, 2016, pp. 241–248.
- [29] Bolgar, I., Scharnowski, S., and Kähler, C., "Passive Flow Control for the Reduction of Load Dynamics Aft of a Backward-Facing Step," *AIAA Journal*, Nov. 2018. doi:10.2514/1.J057274
- [30] Kähler, C., Sammler, B., and Kompenhans, J., "Generation and Control of Particle Size Distributions for Optical Velocity Measurement Techniques in Fluid Mechanics," *Experiments in Fluids*, Vol. 33, No. 6, 2002, pp. 736–742. doi:10.1007/s00348-002-0492-x
- [31] Ragni, D., Schrijer, F., Van Oudheusden, B., and Scarano, F., "Particle Tracer Response Across Shocks Measured by PIV," *Experiments in Fluids*, Vol. 50, No. 1, 2011, pp. 53–64. doi:10.1007/s00348-010-0892-2
- [32] Scharnowski, S., and Kähler, C. J., "On the Loss-of-Correlation Due to PIV Image Noise," *Experiments in Fluids*, Vol. 57, No. 7, 2016, pp. 1–12. doi:10.1007/s00348-016-2203-z
- [33] Scharnowski, S., and Kähler, C., "On the Effect of Curved Streamlines on the Accuracy of PIV Vector Fields," *Experiments in Fluids*, Vol. 54, No. 1, 2013, p. 1435. doi:10.1007/s00348-012-1435-9
- [34] Scharnowski, S., and Kähler, C., "Estimation and Optimization of Loss-of-Pair Uncertainties Based on PIV Correlation Functions," *Experiments in Fluids*, Vol. 57, No. 2, 2016, p. 23. doi:10.1007/s00348-015-2108-2
- [35] Scharnowski, S., Grayson, K., de Silva, C. M., Hutchins, N., Marusic, I., and Kähler, C. J., "Generalization of the PIV Loss-of-Correlation Formula Introduced by Keane and Adrian," *Experiments in Fluids*, Vol. 58, No. 10, 2017, p. 150. doi:10.1007/s00348-017-2431-x
- [36] Westerweel, J., and Scarano, F., "Universal Outlier Detection for PIV Data," *Experiments in Fluids*, Vol. 39, No. 6, 2005, pp. 1096–1100. doi:10.1007/s00348-005-0016-6
- [37] Westerweel, J., Geelhoed, P. F., and Lindken, R., "Single-Pixel Resolution Ensemble Correlation for Micro-PIV Applications," *Experiments in Fluids*, Vol. 37, No. 3, 2004, pp. 375–384. doi:10.1007/s00348-004-0826-y
- [38] Avallone, F., Discetti, S., Astarita, T., and Cardone, G., "Convergence Enhancement of Single-Pixel PIV with Symmetric Double Correlation," *Experiments in Fluids*, Vol. 56, No. 4, 2015, pp. 1–11. doi:10.1007/s00348-015-1938-2
- [39] Kähler, C., Scharnowski, S., and Cierpka, C., "On the Resolution Limit of Digital Particle Image Velocimetry," *Experiments in Fluids*, Vol. 52, No. 6, 2012, pp. 1629–1639. doi:10.1007/s00348-012-1280-x
- [40] Kähler, C., Scharnowski, S., and Cierpka, C., "On the Uncertainty of Digital PIV and PTV Near Walls," *Experiments in Fluids*, Vol. 52, No. 6, 2012, pp. 1641–1656. doi:10.1007/s00348-012-1307-3
- [41] Schlichting, H., and Gersten, K., *Grenzschicht-Theorie*, Springer-Verlag, Berlin, 2006, Chap. 15. doi:10.1007/978-3-662-07554-8
- [42] Scharnowski, S., and Kähler, C., "Investigation of a Transonic Separating/Reattaching Shear Layer by Means of PIV," *Theoretical and Applied Mechanics Letters*, Vol. 5, No. 1, 2015, pp. 30–34. doi:10.1016/j.taml.2014.12.002
- [43] Statnikov, V., Meinke, M., and Schröder, W., "Reduced-Order Analysis of Buffet Flow of Space Launchers," *Journal of Fluid Mechanics*, Vol. 815, March 2017, pp. 1–25. doi:10.1017/jfm.2017.46
- [44] Welch, P. D., "The Use of Fast Fourier Transform for the Estimation of Power Spectra: A Method Based on Time Averaging over Short, Modified Periodograms," *IEEE Transactions on Audio and Electroacoustics*, Vol. 15, No. 2, June 1967, pp. 70–73. doi:10.1109/TAU.1967.1161901
- [45] Marié, S., Deck, S., and Weiss, P., "From Pressure Fluctuations to Dynamic Loads on Axisymmetric Step Flows with Minimal Number of Kulites," *Computers & Fluids*, Vol. 39, No. 5, 2010, pp. 747–755. doi:10.1016/j.compfluid.2009.12.001

D. E. Raveh
Associate Editor